https://doi.org/10.5194/egusphere-2026-2596
Preprint. Discussion started: 17 June 2026

Role of Forest Stand Structure in Groundwater Storage Decline in the Three-North Shelterbelt Forest Region, China

Shu Luo[1], Longhuan Wang[1,2*], Jia Wang[1*], Binghao Jia[2], Rui Han[3], Shaodong Huang[1], Panfei Fang[1], Yujie Li[1], Chu Chu[1], Jianwen Zhang[1]

[1]Beijing Key Laboratory of Precision Forestry, Beijing Forestry University, Beijing, 100083, China
[2]State Key Laboratory of Earth System Numerical Modeling and Application, Institute of Atmospheric Physics, Chinese Academy of Sciences, Beijing, 100029, China
[3]Institute of Environment and Sustainable Development in Agriculture, Chinese Academy of Agricultural Sciences, 100081, Beijing, China

Correspondence to: Longhuan Wang (Email: wanglh202510_cf@bjfu.edu.cn), Jia Wang (Email: wangjia2009@bjfu.edu.cn)

Abstract. Vegetation restoration has significantly altered terrestrial ecosystem dynamics in the Three-North Shelterbelt Forest region (TNSFR), but its impacts on groundwater storage (GWS) remain poorly quantified, particularly as forest stand structure is rarely integrated. This study integrated terrestrial water storage data, land surface model simulation results, and in-situ groundwater observations to assess the spatiotemporal GWS variations. Furthermore, combining meteorological data, forest inventory data, yearbook statistics, and Normalized Difference Vegetation Index (NDVI) data explores how climate and vegetation restoration affect GWS changes. Results show that vegetation restoration in the TNSFR has exhibited a widespread upward trend, with NDVI increasing at an average rate of 0.015 decade^{-1} over the past two decades. Concurrently, GWS has declined significantly with a mean rate of -5.47 mm yr^{-1}, primarily concentrated in regions with substantial increases in forest coverage. In groundwater-dependent ecosystems, monocultures show higher water consumption than mixed forests, and groundwater decline in mature coniferous forests is linked to high-water-consumption spruce species. Structural equation modeling confirms vegetation restoration as the leading anthropogenic driver of GWS decline in the TNSFR. This study highlights the need for tailored ecological strategies for coordinating ecological recovery with sustainable water management in dryland areas.

1 Introduction

Groundwater plays a critical role in human survival by supplying drinking water to billions of people and supporting more than 30% of all irrigated agriculture (McQuillan, 2025). It also serves as a critical buffer against climate change and is indispensable for supporting groundwater-dependent ecosystems (GDEs) (Rohde et al., 2024). However, global groundwater extraction has risen by approximately 50% in the last 50 years (Niazi et al., 2024), and the sustainability of this strategic resource is increasingly threatened by intensive anthropogenic activities and climate change (Li et al., 2022; Rodell et al., 2009), necessitating urgent attention to the spatiotemporal dynamics of groundwater.

https://doi.org/10.5194/egusphere-2026-2596
Preprint. Discussion started: 17 June 2026

The Three-North Shelterbelt Forest region (TNSFR), spanning northern, northeastern, and northwestern China, is characterized primarily by arid and semi-arid climates and covers approximately 42% of China's territory (Chen et al., 2024; Zhang et al., 2025). Due to scarce annual precipitation and intense evapotranspiration, the Three-North Region is inherently characterized by a water deficit (Huang et al., 2017; Xie et al., 2015). Since 1978, the Chinese government has undertaken the Three-North Shelter Forest Program to address desertification and enhance regional environmental and climatic conditions (Yin et al., 2025). It has been documented that forest coverage in this region, which spans 4.07 million km^2, has nearly doubled from 5.05% in 1978 to 9.69% in 2022 (Zheng et al., 2025). However, this region remains characterized by a fragile ecosystem, improper vegetation restoration could actually exacerbate regional water resources scarcity (Hoek van Dijke et al., 2022; Jia et al., 2017; Meng et al., 2020). Beyond the afforestation programs, other anthropogenic activities have further exacerbated groundwater decline. For example, agricultural irrigation has driven substantial groundwater decline in the densely populated North China Plain (Feng et al., 2013), while coal mining has caused significant decline in the mineral-rich Inner Mongolia region (Li et al., 2025).

Traditional groundwater monitoring, which relies on groundwater wells, is often constrained by data paucity, spatiotemporal discontinuities, and restricted accessibility (Jasechko et al., 2024; Taylor et al., 2013). To overcome these limitations, the Gravity Recovery and Climate Experiment (GRACE) satellite mission provides an effective approach by measuring monthly variations in Earth's gravity field, enabling the detection of large-scale terrestrial water storage anomalies (TWSA) (Rodell et al., 2018). GWS anomalies (GWSA) can then be isolated by subtracting simulated canopy water storage, soil moisture and snow water equivalent from TWSA, with these water storage components derived from the Global Land Data Assimilation System (GLDAS) (Rodell et al., 2009; Voss et al., 2013). The integration of GRACE satellite data and GLDAS products has been widely validated for estimating GWS changes across diverse regions, such as South Korea (Karunakalage et al., 2024), the Transboundary Indus Basin (Ali et al., 2022), and Xinjiang in northwestern China (Deng et al., 2025)

The integration of GRACE-based GWSA estimates with human activity data has proven effective in quantifying how climate and human factors affect groundwater (Wu et al., 2020). Several studies have shown that large-area revegetation consumes terrestrial water storage (Zhao et al., 2020). For example, vegetation restoration contributed more to TWSA decline than climate changes in the TNSFR hotspots (Chen et al., 2024). It has also been found to worsen groundwater shortage on the Loess Plateau (Han et al. 2020). However, despite this understanding, research examining the impact of forest stand structure (e.g., age and species composition) on GWS depletion remains scarce, and existing studies are largely confined to plot scales or focus solely on deep soil moisture, thus lacking regional representativeness (Gong et al., 2024; Huang et al., 2023; Shao et al., 2025). Moreover, existing studies assessing single factors like coal mining and irrigation provide valuable insights (Carlson et al., 2025; Xie et al., 2018), but cannot fully quantify how multiple human activities jointly affect GWS across the TNSFR.

As a result, this study aims to: (1) examine the GWS changes driven by vegetation restoration and climatic factors across the TNSFR from 2003 to 2023; (2) assess the impact of vegetation restoration on regional GWS, accounting for variations in stand age and dominant species; and (3) quantify direct and indirect impacts of climate change, vegetation restoration, and other anthropogenic activities for GWSA using Structural Equation Modeling (SEM). The conclusions of this study provide

https://doi.org/10.5194/egusphere-2026-2596
Preprint. Discussion started: 17 June 2026

scientific guidance for achieving a balance between vegetation restoration and the sustainable use of groundwater in dryland regions.

2 Materials and methods

2.1 Study area

The TNSFR encompasses 13 provinces in northeast, north, and northwest China (73°E-128°E, 33°N-50°N), covering an extensive area of 4.069 million km^2 (Chu et al., 2019)(Fig. 1a). The TNSFR accounts for approximately 90% of China's wind-eroded and desertified land, characterized by a fragile ecological environment (Zheng et al., 2025). Since the ecological restoration program began in 1978 (Zhang et al., 2016), the region has experienced significant vegetation greening, making a significant contribution to the overall recovery of China's forest area since the 21st century (Cao, 2011). The TNSFR spans an extensive geographic range. Most areas receive annual precipitation of less than 400 mm, and precipitation shows sharp spatial gradients. The southeast receives over 1100 mm of annual precipitation, compared to less than 50 mm in the northwest (Chen et al., 2024; Meng et al., 2020). For subsequent analysis of climatic impacts, we classified the TNSFR based on Global Aridity Index (AI) (Zomer et al., 2022). We classified the TNSFR into five climate regions (Fig. 1c). Notably, arid and semi-arid regions account for 76.7% of the total study area.

2.2 Datasets

2.2.1 TWSA data

We used monthly TWSA from the Center for Space Research mascon product (CSR-M)(Save et al., 2016) and the Jet Propulsion Laboratory mascon product (JPL-M)(Watkins et al., 2015). Both products were provided on a 0.25° × 0.25° grid. The average of the CSR-M and JPL-M products was used as the TWSA estimate. Monthly data spanning Jan 2003 to Dec 2023 were used in this study. All TWSA data represent surface mass anomalies referenced to the January 2004 – December 2009 mean baseline (Scanlon et al., 2016).

In this study, we used canopy water storage (CWS), soil moisture storage (SMS) and snow water storage (SWS) from the GLDAS-2.1 Noah Land Surface Model (Rodell et al., 2004; Syed et al., 2008), with a spatial resolution of 0.25°. The Noah model simulates soil moisture across four vertical layers (0–10, 10–40, 40–100, and 100–200 cm depth), with total SMS representing the sum of all layers (Syed et al., 2008). All GLDAS variables were expressed as anomalies relative to the same baseline to ensure consistency with TWSA. (Rodell et al., 2007; Yang et al., 2022).

2.2.2 Climate and hydrological data

Monthly precipitation and monthly mean temperature data were obtained from the 1 km resolution climate dataset for China (1901–2024) developed by Peng et al. (2019), available from the National Tibetan Plateau Data Center (https://data.tpdc.ac.cn).

https://doi.org/10.5194/egusphere-2026-2596
Preprint. Discussion started: 17 June 2026

We also obtained monthly ET from the Global Land Evaporation Amsterdam Model (GLEAM) dataset (Miralles et al., 2011, 2025), which has a 0.1° × 0.1° spatial resolution. All meteorological data were converted to a grid of 0.25° × 0.25° resolution.

2.2.3 Land Cover and Vegetation-Related Datasets

The Normalized Difference Vegetation Index (NDVI) data (MOD13C2) were obtained from the Moderate Resolution Imaging Spectroradiometer (MODIS, https://www.earthdata.nasa.gov/data/catalog/lpcloud-mod13c2-061, Didan, K., 2021). This data was acquired at a spatial resolution of 0.05° × 0.05° with a monthly temporal resolution. The NDVI data were also converted to a grid of 0.25° × 0.25° resolution.

Groundwater-dependent ecosystem (GDE) data were obtained from the high-resolution global GDE map developed by Rohde et al. (2024). This product was generated using a random forest model at 1 arcsecond (~30 m) resolution and is hosted on Zenodo (https://doi.org/10.5281/zenodo.11062894).

We used the China Land Cover Dataset to identify the spatiotemporal changes in land use from 2003 to 2023 (Yang and Huang, 2021). Additionally, this study utilized sample plot data from the Ninth National Forest Inventory (NFI, conducted during 2014–2018) to analyze the relationship between forest structural characteristics and GWSA variations.

2.2.4 Socioeconomic data

This study selected four socioeconomic indicators to assess the impact of anthropogenic activities on GWS variations: annual gross domestic product (GDP), annual population, annual irrigated area, and annual coal production. Annual provincial statistical data for GDP (10,000 yuan), population (persons), irrigated area (thousand hectares), and raw coal production (10,000 ton yr^{-1}) were obtained from the China Statistical Yearbook (National Bureau of Statistics, 2004–2024), covering the period from 2003 to 2023. The gridded raw coal production was determined based on coal mine capacity, operational status, and location as provided by Global Energy Monitor (https://globalenergymonitor.org/projects/global-coal-mine-tracker/).

2.3 Methods

2.3.1 Estimating groundwater storage anomalies

Fig. 2 presents the flowchart of this study. GWSA was estimated using a mass balance approach, which can isolate GWSA signals from TWSA by subtracting non-groundwater storage components (Kalu et al., 2025; Zhang et al., 2026). Given that the TNSFR is dominated by arid and semi-arid climates, the long-term variability of surface water storage anomalies (SWSA) is weak, making it negligible compared to GWSA and soil moisture storage anomalies (SMSA) (Ding et al., 2025; Pascal et al., 2022). To align the temporal scales of GRACE and GLDAS, all variables were converted to anomalies using the unified baseline period of January 2004 to December 2009. Therefore, GWSA can be calculated by deducting SMSA, snow water storage anomalies (SWA), and canopy water storage anomalies (CWSA) from TWSA, according to Eq. (1):

$$GWSA = TWSA - SMSA - SWA - CWSA, \quad (1)$$

https://doi.org/10.5194/egusphere-2026-2596
Preprint. Discussion started: 17 June 2026

2.3.2 Validation and uncertainty assessment

GRACE-derived GWSA was compared with the GWSA derived from monitoring data. For this purpose, this study collected data from 21 groundwater monitoring wells from the Geological Environment Monitoring Institute of the China Geological Survey, spanning the period from 2005 to 2016 (Fig. S1). The observed GWSA can be calculated by multiplying groundwater table depth anomaly (GWTDA) by specific yield (Sy) (Bhanja et al., 2016; Gong et al., 2018), as shown in Eq. (2):

$$GWSA = - GWTDA \times Sy, \quad (2)$$

where GWTDA represents the groundwater table depth anomaly, and Sy is the specific yield, with data sourced from Sutanudjaja et al. (2018). To account for the scale mismatch between point-based observations and gridded GRACE-derived GWSA, validation was performed using normalized annual mean series averaged across all available wells, with a focus on the consistency of interannual variability and long-term trend.

In addition, as GWSA is derived by subtracting non-groundwater storage components from TWSA, uncertainties in these individual components may propagate into the final GWSA estimate (Kalu et al., 2025). To address this issue, we used component contribution ratio (CCR) analysis to identify the hydrological component exerting the dominant influence on the residual calculation (Supplementary Text S1). We then evaluated the accuracy of the GLDAS soil moisture product against the European Space Agency Climate Change Initiative (ESA CCI) satellite soil moisture dataset and in situ observations obtained from the China Meteorological Administration (CMA) (Zeng et al., 2025), and additionally compared GLDAS-based SMSA with the fifth generation of European ReAnalysis (ERA5)-derived SMSA. The evaluation focused on time-series consistency, correlation coefficient (R), and root mean square error (RMSE).

2.3.3 Trend analysis

Long-term trends in groundwater storage anomalies (GWSA) and related driving factors were identified using a combination of the Theil–Sen slope estimator (Sen, 1968) and the Mann–Kendall (MK) trend test (Hirsch et al., 1982; Kendall, 1948). These non-parametric methods are less sensitive to seasonal variability and outliers, and are therefore well suited for detecting long-term trends in hydroclimatic time series.

The Theil–Sen slope was employed to capture change trends. The Mann–Kendall test was applied to assess trend significance, with $p \leqslant 0.05$ indicating a significant trend. Based on the sign of the GWSA trend, the study area was further classified into groundwater gain and loss regions for subsequent analyses of climatic change, vegetation restoration, and anthropogenic influences on groundwater dynamics.

2.3.4 Climatic influence analysis

We used precipitation, evapotranspiration, and temperature as the main climatic factors to assess the hydroclimatic controls on GWSA. To characterize regional hydroclimatic water balance, we used net water flux, defined as precipitation minus evapotranspiration (P-ET). This metric provides an indication of the relative amounts of water entering and leaving the system,

https://doi.org/10.5194/egusphere-2026-2596
Preprint. Discussion started: 17 June 2026

allowing it to characterize regional moisture conditions and variations in water availability (Xue and Ullrich, 2022). It provides a useful indicator of the hydroclimatic background under which groundwater changes occur, and was therefore used as the core metric for evaluating the extent to which hydroclimatic conditions explain GWSA variations (Yao et al., 2025).

To assess hydroclimatic influences on groundwater storage change, regional mean time series of GWSA and P−ET anomalies were calculated for the TNSFR, and their long-term trends were compared. Based on the sign of the GWSA trend, temporal variations in GWSA and P−ET anomalies were analyzed separately for groundwater gain and loss subregions. In addition, the study area was classified into aridity zones using the AI. Given that hyper-arid, sub-humid, and humid regions account for a very small share of the total area, the analysis was restricted to arid and semi-arid zones to assess groundwater changes under varying hydroclimatic settings.

2.3.5 Vegetation change and forest structure analysis

We further examined the relationships between vegetation change, forest structural characteristics, and GWSA. Long-term NDVI trends were used to characterize interannual vegetation dynamics (Martínez and Gilabert, 2009; Ukasha et al., 2022). In addition, the China Land Cover Dataset was used to identify changes in major land cover types during 2003–2023 (Chen et al., 2019). Given that GDEs represent ecosystems partially or entirely dependent on groundwater, we used the GDE map as a spatial mask to focus the analysis on ecologically sensitive areas closely linked to groundwater dynamics (Rohde et al., 2024). The original 30 m GDE product was aggregated to the 0.25° grid to generate a GDE mask, and all subsequent vegetation and forest structure analyses were restricted to GDE grid cells. To reduce statistical instability, land cover classes with fewer than 10 resampled grid cells were excluded, leaving five major classes: cropland, forest, grassland, water, and barren land. Forest areas were selected for further analysis, and forest gain and loss zones were distinguished to compare GWSA trend patterns under diverse forest change backgrounds.

Forest inventory indicators derived from the NFI included forest stand structure type, dominant tree species, and mean stand age (Benyon et al., 2017). Since NFI sample plots are distributed at an interval of approximately 4–8 km, plot-level information was first matched to the 0.25° × 0.25° GWSA grid, and stand age and species composition were then aggregated at the grid-cell level. For forest structure analysis, the stand structure classification from the NFI was applied to compare GWSA trends across different stand types and age groups. For tree species analysis, only plots and grid cells dominated by a single species were retained to minimize the confounding effects of mixed forest conditions. Species with insufficient sample size were further excluded, and taxa occupying less than 2% of all grid cells were omitted from subsequent statistics. Based on the filtered samples, variations in GWSA trends were comparatively analyzed across different dominant tree species and stand age conditions (Stelling et al., 2023).

2.3.6 Anthropogenic influence analysis

https://doi.org/10.5194/egusphere-2026-2596
Preprint. Discussion started: 17 June 2026

Since the statistical data were available as provincial-level, they could not be directly compared with GWSA at the 0.25° grid scale. We generated a gridded human activity dataset for the TNSFR by referencing China's grid-based population, irrigation, and GDP datasets (Zhu et al., 2023):

$$Grid_{human} = \frac{S_{province}}{S_{province,ref}} \times Grid_{ref}, \quad (3)$$

where $Grid_{human}$ is the gridded human activity dataset (including irrigation, population, and GDP), $Grid_{ref}$ is the referencing gridded data, $S_{province,ref}$ is the annual data derived from the referencing gridded data, and $S_{province}$ is the annual statistical data from the China Statistical Yearbook.

For raw coal production, provincial totals were allocated to grid cells in proportion to each mine's share of the total coal mine capacity within the corresponding province, while accounting for operational status and location:

$$Grid_{coal} = \frac{Capa}{\sum_{province} Capa} \times S_{province}, \quad (4)$$

where $Grid_{coal}$ is the gridded raw coal production, $Capa$ is the coal mine capacity, $\sum_{province} Capa$ is the provincial coal mine capacity, and $S_{province}$ is the annual statistical raw coal production from the China Statistical Yearbook.

2.3.7 Structural Equation Model

To elucidate how different driving factors directly and indirectly affect GWSA, we applied a SEM using the 'lavaan' package in R (Rosseel, 2012). Unlike traditional regression, it can examine complex links among many variables at once within a unified framework, and allows the representation of latent variables through observed indicators. First, we developed an a priori model based on existing research and theoretical assumptions. Subsequently, all variables were standardized, and we applied variance inflation factor (VIF) tests to check for multicollinearity. Variables with VIF > 10 were excluded, resulting in eight variables retained for model construction, including temperature (TEM), Normalized Difference Vegetation Index (NDVI), irrigation (IRR), evapotranspiration (ET), Gross Domestic Product (GDP), coal (COAL), people (POP) and precipitation (PRE). We finally evaluated SEM fit using CFI, TLI, RMSEA, and SRMR, and obtained the optimal fitting model through iterative refinement and gradually remove non-significant paths.

3 Results

3.1 GWSA changes in the TNSFR

Fig. 3a shows GWS changes displayed divergent variations in different regions of the TNSFR. Notably, 77.06% of the study area experienced significant negative trends in GWS from 2003 to 2023. GWSA showed an increasing trend in the Northeast and Southwest subregions, whereas a decreasing trend in the North China and the Northwest subregions. The maximum annual decline rates of GWSA reaching -40 mm in the Tianshan Mountains and -21.9 mm in North China, respectively.

https://doi.org/10.5194/egusphere-2026-2596
Preprint. Discussion started: 17 June 2026

Fig. 3b shows the normalized annual GWSA during 2005–2016. The GRACE-derived estimates, smoothed with a 3-point moving average, were validated against in-situ observations from 21 monitoring wells across the study area. The estimated GWSA showed a significant declining trend of -0.12 mm yr^{-1}, consistent with the observed trend of -0.08 mm yr^{-1}. Among the 21 wells (Fig. S1), 16 (76.2%) exhibited consistent trends between observed and estimated values, of which 10 (47.6%) showed statistically significant declining trends in both datasets ($p < 0.05$). This result suggests that the GRACE/GLDAS-based GWSA successfully monitors groundwater changes in the TNSFR.

In addition to the validation described above, supplementary validation was conducted for SMSA to further assess the robustness of the GWSA estimates. The CCR analysis showed that SMSA was the dominant GLDAS-derived hydrological storage component, with a contribution ratio of 84.85 % (Supplementary Fig. S2). Accordingly, subsequent validation focused primarily on SMSA. First, the performance of GLDAS and ERA5 in capturing the spatiotemporal variability of surface soil moisture was evaluated against the ESA CCI satellite soil moisture product. Figure S3 shows the mean time series of surface soil water from ESA CCI, ERA5, and GLDAS during 2003–2023. The results indicated that although both ERA5 and GLDAS could capture the spatiotemporal dynamics of soil water, GLDAS showed higher consistency with ESA CCI. At the temporal scale, the correlation coefficient between GLDAS and ESA CCI was 0.834, which was 0.13 higher than that of ERA5, accompanied by a lower RMSE (0.012 $m^3\ m^{-3}$). At the spatial scale (Supplementary Fig. S4), the correlation coefficient between ERA5 and ESA CCI was 0.530, whereas that between GLDAS and ESA CCI reached 0.554. Spatial comparisons further demonstrated that GLDAS achieved higher consistency and smaller errors across most of the study area. Furthermore, station-based validation suggested that for both surface (0–10 cm) and root-zone (0–100 cm) soil moisture, GLDAS outperformed ERA5 in terms of both correlation (R=0.397; R=0.255) and error metrics (RMSE=0.083 $m^3\ m^{-3}$; RMSE=0.082 $m^3\ m^{-3}$) (Supplementary Fig. S5). Collectively, both the satellite product and in situ observations support the reliability of GLDAS for SMSA estimation and subsequent GWSA derivation.

Fig.4a presents the monthly time series of GWSA during 2003-2023. GWS in the TNSFR declined significantly at -5.47 mm·yr^{-1}. Specifically, the average decline rate in GWS loss regions reached 8.56 mm yr^{-1}. GWS in the TNSFR showed a relatively stable trend with minor fluctuations during 2003–2008. Notably, GWS showed a significant decrease since 2009. Comparison with the net water flux time series revealed a growing divergence, suggesting that GWSA in the TNSFR has been increasingly influenced by human activities.

3.2 Impact of climate change on GWS

Following the water balance principle, this study examined GWS changes under the context of climate change by analyzing P-ET as an indicator of regional wetness and dryness. Fig. 4b shows the temporal variations of P-ET in the TNSFR from 2003 to 2023, with results indicating that the overall net water flux in the region remained basically stable, with a minimal change trend of 0.004 mm $month^{-1}$ (black line). This suggests that climatic factors in the region have undergone minimal changes over the past two decades. Furthermore, the TNSFR was categorized into GWS gain and loss areas based on the sign of the GWS time series trends. We further analyzed the time series trends of net water flux in these two sub-regions (Fig. 4b). In the GWS

https://doi.org/10.5194/egusphere-2026-2596
Preprint. Discussion started: 17 June 2026

gain area (blue line), net water flux rose at 0.037 mm yr^{-1}. In the GWS loss area (red line), it fell at -0.006 mm yr^{-1}. Notably, GWS changes are relatively consistent with the rising and falling trends of P-ET. This synchrony suggests that climatic drivers are the primary factors controlling GWS change in the TNSFR.

The analysis excluded hyper-arid, sub-humid, and humid regions due to their minimal grid-area representation, focusing instead on arid and semi-arid areas. In the arid region, the ET trend within the greening areas (−0.48 mm yr^{-1}) was higher than the regional average (−0.66 mm yr^{-1}). The region exhibited an insignificant decreasing trend in precipitation (−0.54 mm yr^{-1}), leading to a decreasing trend in regional ET. As both changes were statistically insignificant, the P−ET budget remained relatively stable with only marginal change. Furthermore, since approximately 60% of the greening occurred over bare land or extremely sparse vegetation that primarily consumes soil moisture rather than tapping groundwater (Feldman et al., 2023), GWS in this region declined at a substantially lower rate (−5.18 mm yr^{-1}) than that in the semi-arid region (−9.66 mm yr^{-1}; Fig. 5), representing a 1.86-fold difference in the magnitude of decline despite the presence of irrigation (Fig. 9).

By contrast, greening in semi-arid regions was dominated by grassland greening, localized forest greening, and grassland-to-forest conversion, which together accounted for approximately 73% of the total semi-arid area. These areas were also commonly subject to intensive agricultural production and coal-mining activities (Fig. 9). Although precipitation increased at a rate of 2.374 mm yr^{-1}, ET exhibited a significant increase of 1.797 mm yr^{-1}, resulting in only a limited change in P−ET. Therefore, the more pronounced decline in GWS in semi-arid regions was associated with the combined influences of climate variability, vegetation greening, and anthropogenic water use.

3.3 Impact of vegetation restoration on GWS

In the last 30 years, over 40% of vegetated land saw ongoing greening. After 2000, vegetation recovered notably in the Loess Plateau, Hulunbuir Desert, and oasis areas of northwestern China (Cai et al., 2020). Fig. 6a illustrates that NDVI increased at an average rate of 0.015 $decade^{-1}$ from 2003 to 2023, with three primary greening hotspots identified: the Loess Plateau, Northeast China, and the central Tianshan Mountains. Fig. 6b shows that during 2003–2023, the magnitude of GWS trends in forest expansion areas (-9.16 mm yr^{-1}) was 31.8% greater than that in forest loss areas (-6.95 mm yr^{-1}) and 41% greater than that in areas of grassland expansion (−6.50 mm yr^{-1}). Land use change data (Fig. 6c-i) show that forest cover increased most dramatically over the past two decades, expanding by 44.4% compared to 2003. Given this trend, we focus our subsequent analysis on how forest dynamics and stand structure affect GWSA. Previous studies have demonstrated that afforestation activities in China's forested regions have led to substantial groundwater level declines (Lu et al., 2018).

To further investigate how forest structure type and stand age affect GWS, we analyzed GWSA trends across different forest structure categories using the Ninth NFI data (Fig. 7). The results revealed that pure forests exhibited more pronounced groundwater depletion than mixed forests. Specifically, conifer pure stands (CP) showed the most negative GWSA trends, reaching a peak of -1.06 mm $month^{-1}$ at the mature stage, which was significantly higher than that of conifer mixed stands (CM, -0.31 mm $month^{-1}$) and broadleaf pure stands (BP, -0.67 mm $month^{-1}$) at the same age class. Mixed forests have been found to mitigate deep soil water shortages through variation in root water uptake among different species. (Dai et al., 2023).

https://doi.org/10.5194/egusphere-2026-2596
Preprint. Discussion started: 17 June 2026

Furthermore, the effect of stand age on groundwater consumption varied with forest structure type. For conifer pure stands, groundwater depletion peaked at the mature stage (-1.06 mm month^{-1}) and slightly recovered at the over-mature stage (-0.92 mm month^{-1}). Notably, conifer-broadleaf mixed stands (CBM) exhibited a pronounced decreasing trend with increasing stand age, declining from -1.25 mm month^{-1} in young forests to -0.55 mm month^{-1} in over-mature forests, representing a 56% reduction.

Species composition also exerted a significant influence on GWS dynamics. To eliminate the confounding effects of multi-species mixing, only monospecific plots were included in this analysis, accounting for 80.1% of total sample plots (Fig. 8a-b). Spatially, forests in the TNSFR were dominated by conifers (74.9%), exhibiting distinct geographical differentiation (Fig. 8a). Spruce was predominantly distributed in the Tianshan and Qilian mountain ranges, larch occurred in the northern Tianshan slopes and the Greater Khingan Mountains, Chinese pine was located in the Yanshan-Taihang mountain region, while broadleaf forests represented by poplar were common in the central Loess Plateau and northern North China.

Groundwater consumption characteristics differed substantially among tree species (Fig. 8b). Coniferous forests generally exhibited stronger groundwater depletion than broadleaf forests, with GWSA trends showing an increasing tendency with stand age. Spruce displayed the strongest groundwater consumption at the mature stage (100–200 years), with GWSA trends reaching -3 to -4 mm month^{-1}. Notably, spruce accounted for 63.9% of coniferous forest plots, representing the dominant conifer species in the TNSFR. In contrast, cypress, despite having stand ages of 250–400 years, exhibited GWSA trends approaching zero. Additionally, poplar forests were generally younger and showed relatively stable groundwater consumption that was lower than that of coniferous forests.

In summary, conifer pure stands dominated by spruce constitute a major driver of GWS decline in the TNSFR. Our results show that adjustments to forest composition, particularly expanding mixed forest coverage and optimizing species configuration, can provide new insights for sustainable groundwater management locally.

3.4 Quantitative analysis of the drivers of GWS

The SEM fit indices indicated good reliability (CFI = 0.973, TLI = 0.926, RMSEA = 0.065, SRMR = 0.025; Fig. 10a). Results showed that climate remains the dominant factor influencing GWS. Temperature exhibited the highest total effect (-57.6%), with direct effects accounting for -56.4%, indicating that climate warming exerts a significant negative impact on GWS. Existing studies have confirmed that rising temperatures intensify groundwater depletion by enhancing evapotranspiration processes (Condon et al., 2020).

Among anthropogenic factors, NDVI emerged as the primary driver affecting GWSA, with a total effect of -20.5%. While extensive revegetation efforts have substantially improved ecological conditions, the associated impacts on regional water resources should not be overlooked. This finding is consistent with related studies on the Loess Plateau, which indicated that vegetation restoration programs may create conflicts in water resource demands between human society and ecosystems (Feng et al., 2016). In addition, irrigation have a significant effect on GWS changes. The TNSFR encompasses several important agricultural irrigation zones where groundwater supports crop production, but long-term large-scale extraction has led to

https://doi.org/10.5194/egusphere-2026-2596
Preprint. Discussion started: 17 June 2026

sustained groundwater level decline (Hu et al., 2016). Notably, agricultural water use exerts multiple impacts on groundwater systems: on one hand, it directly extracts groundwater resources; on the other hand, it indirectly intensifies water loss by promoting crop growth and enhancing vegetation transpiration (Condon and Maxwell, 2019).

4 Discussion

4.1 Implications for water resources management and land surface model development

Numerous studies have shown that changes in GWS are influenced by vegetation restoration and vary depending on forest stand structure (Jia et al., 2017; Wang et al., 2020). Our results revealed that forest structure significantly influences GWS changes in the TNSFR. Conifer pure stands, particularly those dominated by spruce, exhibited the strongest groundwater depletion, reaching -3 to -4 mm month-1 at the mature stage, while mixed forests showed considerably lower water consumption (-0.31 mm month-1). Monoculture plantations typically exhibit higher water consumption than mixed forests in arid and semi-arid regions. The core ecological mechanism underlying this phenomenon is that intraspecific competition is, on average, 4 to 5 times stronger than competition between species (Adler et al., 2018). By contrast, mixed forests can significantly enhance soil water use efficiency under environmental stress through complementarity effects (Gong et al., 2024). These results suggest that future afforestation programs in the TNSFR should optimize forest structure by increasing the proportion of mixed forests and selecting species with lower water consumption to balance ecological benefits with groundwater sustainability.

Beyond vegetation restoration impacts, GWS decline in the TNSFR is also driven by anthropogenic activities, particularly agricultural irrigation and coal mining. Fig 9a-c shows that the hotspots of agricultural irrigation and coal mining are concentrated in the North China Plain and the northwestern region. Earlier research has linked GWS decline in northwestern China to growing agricultural water extraction and demographic pressures, reporting groundwater loss rates of up to -3 cm yr^{-1} (Cheng et al., 2023). Furthermore, provinces such as Shanxi, Inner Mongolia, and Shaanxi are major energy production bases in China, where extensive coal mining operations are conducted annually. However, the disruption of aquifer systems caused by mine dewatering and industrial water consumption has resulted in substantial GWS losses (Xie et al., 2018). The Chinese government began to shut down coal mines in 2010. (Ma et al., 2024) found that mine closures can help TWS recover quickly, with an average increase of 18.8 ± 8.9 mm yr^{-1}. Despite these policy interventions, the legacy effects of decades of intensive mining and irrigation have caused persistent damage to aquifer systems. Groundwater replenishment is slow in dry regions, and recovery from depletion takes even longer (Jasechko et al., 2024). These results indicate that groundwater depletion is still serious in the TNSFR, calling for better water resource management to balance vegetation restoration with groundwater sustainability.

Our results demonstrate that both species composition and stand age structure significantly influence groundwater storage dynamics. However, most current land surface models treat forested areas as homogeneous land cover types, classifying forests solely on the basis of vegetation cover fraction or simple plant functional types, and thus fail to capture the regulatory effects

https://doi.org/10.5194/egusphere-2026-2596
Preprint. Discussion started: 17 June 2026

of different tree species and stand ages on root distribution and water use characteristics. This simplification prevents models from adequately representing the differences in water consumption among various forest types when simulating GWS changes, and may therefore systematically underestimate the risk of groundwater depletion induced by afforestation. To reliably assess the hydrological sustainability of dryland afforestation at the global scale, the development of land surface models urgently needs to incorporate forest stand structure modules, including species-specific physiological traits, age-dependent root distributions, and complementarity effects in mixed forests. Improving these components will not only enhance the simulation accuracy of models under dryland afforestation scenarios, but also provide policymakers worldwide with more reliable tools for groundwater risk assessment.

4.2 Uncertainties and limitations

Previous studies have demonstrated that GRACE datasets from different organizations contain inherent uncertainties, and the derived TWSA estimates vary depending on the solutions and spatial scales (Ferreira et al., 2016; Shamsudduha and Taylor, 2020). Monthly TWSA data were obtained from two GRACE products (CSR-M and JPL-M) in this study. Averaging the two datasets helped to mitigate uncertainties associated with differences between GRACE products (Wang et al., 2024).

To assess the influence of GRACE product choice, we compared the GWSA estimates derived separately from two GRACE products. The GWSA derived from the two products shows similar spatial patterns in both the multi-year mean and long-term trend maps (Supplementary Figs. S4 and S5). The main spatial contrasts are retained in the two products, although local differences remain in the magnitude of the trends. The regional mean GWSA trend derived from the two products is -5.472 $\pm$ 0.098 mm yr^{-1} (Supplementary Text S4) (Zou et al., 2022). This small uncertainty suggests that differences between CSR-M and JPL-M have a limited effect on the regional GWSA trend in the TNSFR, supporting the robustness of the averaged GWSA estimate.

Beyond uncertainties in the GRACE-derived GWSA estimates, the quantification of human impacts on GWS also faces challenges. It should be noted that we used irrigated area and raw coal production as proxy indicators to assess the impacts of agricultural irrigation and coal mining on GWS, rather than converting them to actual water consumption. This approach was adopted for two main reasons. First, water consumption coefficients exhibit significant regional differences in China (Li et al., 2020). Also, current methods for estimating water use have uncertainties because of limited data and model limitations (Liu et al., 2024). Second, water consumption in coal mining involves multiple industrial processes including extraction, washing, cooling, dust suppression, and wastewater treatment, making it difficult to accurately quantify water use at each production stage (Meißner, 2021). Furthermore, this study mainly examines how vegetation restoration affects GWS, while agricultural irrigation and coal mining are discussed as supplementary anthropogenic factors.

To investigate the variations in GWSA across different tree species and stand ages, this study conducted analyses based on the 9th NFI data. Although the use of single-period rather than multi-period forest inventory data may affect the accuracy of stand age determination, this limitation can be effectively mitigated given the characteristics of the dominant tree species in the TNSFR. The predominant species are spruce and poplar. According to the Technical Regulations for National Forest

https://doi.org/10.5194/egusphere-2026-2596
Preprint. Discussion started: 17 June 2026

Continuous Inventory, spruce plantations in northern China are grouped in 20-year age intervals. Since this aligns with the 2003–2023 study period, using single-period inventory data has little effect on the age classification of spruce forests. For poplar forests, over 80% of stands fall within the 20–40 years age range, with the vast majority classified as mature or over-mature forests. Although the age group interval for poplar is 10 years, the core objective of this research is to infer the relationship between GWSA and the spatial heterogeneity of tree species and stand age, rather than relying on precise annual age sequences, therefore the methodology is reasonable. Additionally, it is worth highlighting that the TNSFR has experienced a steady increase in forest coverage in the last 50 years, through measures encompassing natural vegetation enclosure and artificial afforestation. Given that this process integrates human facilitation with policy-influenced natural recovery, vegetation restoration is treated as an anthropogenic driver in this study.

Finally, one more caveat should be noted. This study did not account for land-atmosphere interactions on regional water cycling. Previous work examining the hydrological consequences of vegetation change often disregarded vegetation–precipitation feedbacks, preventing a full representation of the processes by which vegetation regulates regional precipitation through transpiration. (Li et al., 2018). Future work will use land-atmosphere coupled models to separate vegetation's direct impacts on evapotranspiration from indirect effects via atmospheric circulation and moisture recycling (Zan et al., 2024; Zemp et al., 2017). This will help better understand how vegetation affects groundwater.

5 Conclusion

This study utilized GRACE satellite data and GLDAS model simulations to characterize the spatiotemporal variations and the drivers affecting GWS dynamics in the TNSFR from 2003 to 2023. Results indicate that GWS decreased by -5.47 mm yr^{-1} on average. We also found that due to large-scale implementation of ecological restoration programs, the Loess Plateau, Northeast China, and the central Tianshan Mountains in Xinjiang experienced significant forest recovery. Concurrently, the GWS decline rate in forest gain areas was 31.8% higher than that in forest loss areas. In groundwater-dependent ecosystems, monocultures exhibited higher water consumption than mixed forests, and groundwater decline in mature coniferous forests was linked to high-water-consumption spruce species. Attribution analysis using SEM revealed that climatic factors remain the dominant drivers of GWS at large scales, while vegetation restoration emerged as the primary anthropogenic driver affecting GWS. This study highlights that ecological restoration projects need to optimize forest stand structure and rationally allocate tree species to achieve synergies between ecological benefits and groundwater resource conservation.

Data availability

All the data sources have been stated in the manuscript.

https://doi.org/10.5194/egusphere-2026-2596
Preprint. Discussion started: 17 June 2026

Author contributions

The CRediT contributor roles are as follows:

Shu Luo: Writing – original draft, Formal analysis, Data curation ,Methodology, Visualization, Investigation.

Longhuan Wang: Conceptualization, Writing – review & editing, Supervision, Funding acquisition, Project administration.

Jia Wang: Writing – review & editing, Supervision, Funding acquisition.

Binghao Jia: Resources, Investigation.

Rui Han: Data curation, Investigation.

Shaodong Huang: Data curation, Methodology.

Panfei Fang: Data curation, Methodology.

Yujie Li: Data curation, Methodology.

Chu Chu: Data curation, Methodology.

Jianwen Zhang: Data curation, Methodology.

Competing interests

The authors declare that they have no known competing financial interests or personal relationships that could have appeared to influence the work reported in this paper.

Acknowledgements

This work was jointly supported by the National Natural Science Foundation of China (42575183, 42330507, 42542104, U24A20573) and the Fundamental Research Funds for the Central Universities (XJJSKYQD202516).

References

Adler, P. B., Smull, D., Beard, K. H., Choi, R. T., Furniss, T., Kulmatiski, A., Meiners, J. M., Tredennick, A. T., and Veblen, K. E.: Competition and coexistence in plant communities: Intraspecific competition is stronger than interspecific competition, Ecol. Lett., 21, 1319–1329, https://doi.org/10.1111/ele.13098, 2018.

https://doi.org/10.5194/egusphere-2026-2596
Preprint. Discussion started: 17 June 2026

Ali, S., Wang, Q., Liu, D., Fu, Q., Mafuzur Rahaman, Md., Abrar Faiz, M., and Jehanzeb Masud Cheema, M.: Estimation of spatio-temporal groundwater storage variations in the lower transboundary indus basin using GRACE satellite, J. Hydrol., 605, 127315, https://doi.org/10.1016/j.jhydrol.2021.127315, 2022.

Benyon, R. G., Nolan, R. H., Hawthorn, S. N. D., and Lane, P. N. J.: Stand-level variation in evapotranspiration in non-water-limited eucalypt forests, J. Hydrol., 551, 233–244, https://doi.org/10.1016/j.jhydrol.2017.06.002, 2017.

Bhanja, S. N., Mukherjee, A., Saha, D., Velicogna, I., and Famiglietti, J. S.: Validation of GRACE based groundwater storage anomaly using in-situ groundwater level measurements in India, J. Hydrol., 543, 729–738, https://doi.org/10.1016/j.jhydrol.2016.10.042, 2016.

Cai, D., Ge, Q., Wang, X., Liu, B., Goudie, A. S., and Hu, S.: Contributions of ecological programs to vegetation restoration in arid and semiarid China, Environ. Res. Lett., 15, 114046, https://doi.org/10.1088/1748-9326/abbde9, 2020.

Cao, S.: Impact of China's large-scale ecological restoration program on the environment and society in arid and semiarid areas of china: Achievements, problems, synthesis, and applications, Critical Reviews in Environmental Science and Technology, 41, 317–335, https://doi.org/10.1080/10643380902800034, 2011.

Carlson, G., Massari, C., Rotiroti, M., Bonomi, T., Preziosi, E., Wilder, A., Whitaker, D., and Girotto, M.: Intensive irrigation buffers groundwater declines in key european breadbasket, Nat Water, 3, 683–692, https://doi.org/10.1038/s44221-025-00445-4, 2025.

Chen, A., Xiong, J., Wu, S., and Yang, Y.: Changes in terrestrial water storage in the three-north region of China over 2003–2021: Assessing the roles of climate and vegetation restoration, J. Hydrol., 637, 131303, https://doi.org/10.1016/j.jhydrol.2024.131303, 2024.

Chen, C., Park, T., Wang, X., Piao, S., Xu, B., Chaturvedi, R. K., Fuchs, R., Brovkin, V., Ciais, P., Fensholt, R., Tømmervik, H., Bala, G., Zhu, Z., Nemani, R. R., and Myneni, R. B.: China and India lead in greening of the world through land-use management, Nat. Sustainability, 2, 122–129, https://doi.org/10.1038/s41893-019-0220-7, 2019.

Cheng, W., Feng, Q., Xi, H., Yin, X., Sindikubwabo, C., Habiyakare, T., Chen, Y., and Zhao, X.: Spatiotemporal variability and controlling factors of groundwater depletion in endorheic basins of northwest China, J. Environ. Manage., 344, 118468, https://doi.org/10.1016/j.jenvman.2023.118468, 2023.

Chu, X., Zhan, J., Li, Z., Zhang, F., and Qi, W.: Assessment on forest carbon sequestration in the three-north shelterbelt program region, China, J. Cleaner Prod., 215, 382–389, https://doi.org/10.1016/j.jclepro.2018.12.296, 2019.

Condon, L. E. and Maxwell, R. M.: Simulating the sensitivity of evapotranspiration and streamflow to large-scale groundwater depletion, Sci. Adv., 5, eaav4574, https://doi.org/10.1126/sciadv.aav4574, 2019.

Condon, L. E., Atchley, A. L., and Maxwell, R. M.: Evapotranspiration depletes groundwater under warming over the contiguous united states, Nat. Commun., 11, 873, https://doi.org/10.1038/s41467-020-14688-0, 2020.

Dai, J., Li, Y., and Wang, L.: Mixed-species plantations alleviate deep soil water depletion and facilitate hydrological niche partitioning compared to pure plantations, For. Ecol. Manage., 539, 121017, https://doi.org/10.1016/j.foreco.2023.121017, 2023.

Deng, X., Wang, G., Han, F., Gong, Y., Hao, X., Zhang, G., Zhang, P., and Shan, Q.: Groundwater storage anomalies projection by optimized deep learning refines groundwater management in typical arid basins, J. Hydrol., 649, 132452, https://doi.org/10.1016/j.jhydrol.2024.132452, 2025.

https://doi.org/10.5194/egusphere-2026-2596
Preprint. Discussion started: 17 June 2026

Didan, K.: MODIS/Terra Vegetation Indices Monthly L3 Global 0.05Deg CMG V061, https://doi.org/10.5067/MODIS/MOD13C2.061, 2021.

Ding, K., Zhao, X., Cheng, J., Yu, Y., Luo, Y., Couchot, J., Zheng, K., Lin, Y., and Wang, Y.: GRACE/ML-based analysis of the spatiotemporal variations of groundwater storage in Africa, Journal of Hydrology, 647, 132336, https://doi.org/10.1016/j.jhydrol.2024.132336, 2025.

Feldman, A. F., Short Gianotti, D. J., Dong, J., Akbar, R., Crow, W. T., McColl, K. A., Konings, A. G., Nippert, J. B., Tumber-Dávila, S. J., Holbrook, N. M., Rockwell, F. E., Scott, R. L., Reichle, R. H., Chatterjee, A., Joiner, J., Poulter, B., and Entekhabi, D.: Remotely sensed soil moisture can capture dynamics relevant to plant water uptake, Water Resources Research, 59, e2022WR033814, https://doi.org/10.1029/2022WR033814, 2023.

Feng, W., Zhong, M., Lemoine, J.-M., Biancale, R., Hsu, H.-T., and Xia, J.: Evaluation of groundwater depletion in north China using the gravity recovery and climate experiment (GRACE) data and ground-based measurements, Water Resour. Res., 49, 2110–2118, https://doi.org/10.1002/wrcr.20192, 2013.

Feng, X., Fu, B., Piao, S., Wang, S., Ciais, P., Zeng, Z., Lü, Y., Zeng, Y., Li, Y., Jiang, X., and Wu, B.: Revegetation in China's loess plateau is approaching sustainable water resource limits, Nat. Clim. Change, 6, 1019–1022, https://doi.org/10.1038/nclimate3092, 2016.

Ferreira, V. G., Montecino, H. D. C., Yakubu, C. I., and Heck, B.: Uncertainties of the gravity recovery and climate experiment time-variable gravity-field solutions based on three-cornered hat method, J. Appl. Remote Sens., 10, 015015, https://doi.org/10.1117/1.JRS.10.015015, 2016.

Gong, C., Tan, Q., Liu, G., and Xu, M.: Positive effects of mixed-species plantations on soil water storage across the Chinese loess plateau, For. Ecol. Manage., 552, 121571, https://doi.org/10.1016/j.foreco.2023.121571, 2024.

Gong, H., Pan, Y., Zheng, L., Li, X., Zhu, L., Zhang, C., Huang, Z., Li, Z., Wang, H., and Zhou, C.: Long-term groundwater storage changes and land subsidence development in the north China plain (1971–2015), Hydrogeol. J., 26, 1417–1427, https://doi.org/10.1007/s10040-018-1768-4, 2018.

Han, Z., Huang, S., Huang, Q., Bai, Q., Leng, G., Wang, H., Zhao, J., Wei, X., and Zheng, X.: Effects of vegetation restoration on groundwater drought in the loess plateau, China, Journal of Hydrology, 591, 125566, https://doi.org/10.1016/j.jhydrol.2020.125566, 2020.

Hirsch, R. M., Slack, J. R., and Smith, R. A.: Techniques of trend analysis for monthly water quality data, Water Resources Research, 18, 107–121, https://doi.org/10.1029/WR018i001p00107, 1982.

Hoek van Dijke, A. J., Herold, M., Mallick, K., Benedict, I., Machwitz, M., Schlerf, M., Pranindita, A., Theeuwen, J. J. E., Bastin, J.-F., and Teuling, A. J.: Shifts in regional water availability due to global tree restoration, Nat. Geosci., 15, 363–368, https://doi.org/10.1038/s41561-022-00935-0, 2022.

Hu, X., Shi, L., Zeng, J., Yang, J., Zha, Y., Yao, Y., and Cao, G.: Estimation of actual irrigation amount and its impact on groundwater depletion: A case study in the hebei plain, China, J. Hydrol., 543, 433–449, https://doi.org/10.1016/j.jhydrol.2016.10.020, 2016.

Huang, J., Li, Y., Fu, C., Chen, F., Fu, Q., Dai, A., Shinoda, M., Ma, Z., Guo, W., Li, Z., Zhang, L., Liu, Y., Yu, H., He, Y., Xie, Y., Guan, X., Ji, M., Lin, L., Wang, S., Yan, H., and Wang, G.: Dryland climate change: Recent progress and challenges, Rev. Geophys., 55, 719–778, https://doi.org/10.1002/2016RG000550, 2017.

https://doi.org/10.5194/egusphere-2026-2596
Preprint. Discussion started: 17 June 2026

Huang, L., Pei, Y., Shao, M., Jia, X., Tang, X., Zhang, Y., and Pan, Y.: Multi-species plantation intensifies soil water competition and groundwater depletion in a water-limited desert region, For. Ecol. Manage., 537, 120953, https://doi.org/10.1016/j.foreco.2023.120953, 2023.

Jasechko, S., Seybold, H., Perrone, D., Fan, Y., Shamsudduha, M., Taylor, R. G., Fallatah, O., and Kirchner, J. W.: Rapid groundwater decline and some cases of recovery in aquifers globally, Nature, 625, 715–721, https://doi.org/10.1038/s41586-023-06879-8, 2024.

Jia, X., Shao, M., Zhu, Y., and Luo, Y.: Soil moisture decline due to afforestation across the Loess Plateau, China, Journal of Hydrology, 546, 113–122, https://doi.org/10.1016/j.jhydrol.2017.01.011, 2017.

Kalu, I., Ndehedehe, C. E., Ferreira, V. G., Janardhanan, S., and Kennard, M. J.: Unravelling soil moisture uncertainties in GRACE groundwater modelling, J. Hydrol., 650, 132489, https://doi.org/10.1016/j.jhydrol.2024.132489, 2025.

Karunakalage, A., Lee, J.-Y., Daqiq, M. T., Cha, J., Jang, J., and Kannaujiya, S.: Characterization of groundwater drought and understanding of climatic impact on groundwater resources in korea, J. Hydrol., 634, 131014, https://doi.org/10.1016/j.jhydrol.2024.131014, 2024.

Kendall, M. G.: Rank correlation methods, C. Griffin, 178 pp., 1948.

Li, X., Jiang, W., and Duan, D.: Spatio-temporal analysis of irrigation water use coefficients in China, J. Environ. Manage., 262, 110242, https://doi.org/10.1016/j.jenvman.2020.110242, 2020.

Li, X., Long, D., Scanlon, B. R., Mann, M. E., Li, X., Tian, F., Sun, Z., and Wang, G.: Climate change threatens terrestrial water storage over the tibetan plateau, Nat. Clim. Change, 12, 801–807, https://doi.org/10.1038/s41558-022-01443-0, 2022.

Li, X., Du, S., Hu, S., Dong, D., Jiang, D., Cao, C., Lin, G., and Fu, J.: Simulation of surface water–groundwater interaction in coal mining subsidence areas: A case study of the kuye river basin in China, J. Hydrol., 659, 133243, https://doi.org/10.1016/j.jhydrol.2025.133243, 2025.

Li, Y., Piao, S., Li, L. Z. X., Chen, A., Wang, X., Ciais, P., Huang, L., Lian, X., Peng, S., Zeng, Z., Wang, K., and Zhou, L.: Divergent hydrological response to large-scale afforestation and vegetation greening in China, Sci. Adv., 4, eaar4182, https://doi.org/10.1126/sciadv.aar4182, 2018.

Liu, K., Bo, Y., Li, X., Wang, S., and Zhou, G.: Uncovering current and future variations of irrigation water use across China using machine learning, Earth's Future, 12, e2023EF003562, https://doi.org/10.1029/2023EF003562, 2024.

Lu, C., Zhao, T., Shi, X., and Cao, S.: Ecological restoration by afforestation may increase groundwater depth and create potentially large ecological and water opportunity costs in arid and semiarid China, J. Cleaner Prod., 176, 1213–1222, https://doi.org/10.1016/j.jclepro.2016.03.046, 2018.

Ma, R., Gao, J., Guan, C., and Zhang, B.: Coal mine closure substantially increases terrestrial water storage in China, Commun. Earth Environ., 5, 418, https://doi.org/10.1038/s43247-024-01589-z, 2024.

Martínez, B. and Gilabert, M. A.: Vegetation dynamics from NDVI time series analysis using the wavelet transform, Remote Sens. Environ., 113, 1823–1842, https://doi.org/10.1016/j.rse.2009.04.016, 2009.

McQuillan, C.: Groundwater depletion in a drying world, The Lancet Planetary Health, 9, https://doi.org/10.1016/j.lanplh.2025.101372, 2025.

https://doi.org/10.5194/egusphere-2026-2596
Preprint. Discussion started: 17 June 2026

Meißner, S.: The impact of metal mining on global water stress and regional carrying capacities—a GIS-based water impact assessment, Resources, 10, 120, https://doi.org/10.3390/resources10120120, 2021.

Meng, S., Xie, X., Zhu, B., and Wang, Y.: The relative contribution of vegetation greening to the hydrological cycle in the three-north region of China: A modelling analysis, J. Hydrol., 591, 125689, https://doi.org/10.1016/j.jhydrol.2020.125689, 2020.

Miralles, D. G., Holmes, T. R. H., De Jeu, R. a. M., Gash, J. H., Meesters, A. G. C. A., and Dolman, A. J.: Global land-surface evaporation estimated from satellite-based observations, Hydrol. Earth Syst. Sci., 15, 453–469, https://doi.org/10.5194/hess-15-453-2011, 2011.

Miralles, D. G., Bonte, O., Koppa, A., Baez-Villanueva, O. M., Tronquo, E., Zhong, F., Beck, H. E., Hulsman, P., Dorigo, W., Verhoest, N. E. C., and Haghdoost, S.: GLEAM4: Global land evaporation and soil moisture dataset at 0.1° resolution from 1980 to near present, Sci. Data, 12, 416, https://doi.org/10.1038/s41597-025-04610-y, 2025.

Niazi, H., Wild, T. B., Turner, S. W. D., Graham, N. T., Hejazi, M., Msangi, S., Kim, S., Lamontagne, J. R., and Zhao, M.: Global peak water limit of future groundwater withdrawals, Nat. Sustainability, 7, 413–422, https://doi.org/10.1038/s41893-024-01306-w, 2024.

Pascal, C., Ferrant, S., Selles, A., Maréchal, J.-C., Paswan, A., and Merlin, O.: Evaluating downscaling methods of GRACE (gravity recovery and climate experiment) data: A case study over a fractured crystalline aquifer in southern India, Hydrology and Earth System Sciences, 26, 4169–4186, https://doi.org/10.5194/hess-26-4169-2022, 2022.

Peng, S., Ding, Y., Liu, W., and Li, Z.: 1 km monthly temperature and precipitation dataset for China from 1901 to 2017, Earth Syst. Sci. Data, 11, 1931–1946, https://doi.org/10.5194/essd-11-1931-2019, 2019.

Rodell, M., Houser, P. R., Jambor, U., Gottschalck, J., Mitchell, K., Meng, C.-J., Arsenault, K., Cosgrove, B., Radakovich, J., Bosilovich, M., Entin, J. K., Walker, J. P., Lohmann, D., and Toll, D.: The global land data assimilation system, Bull. Am. Meteorol. Soc., 85, 381–394, https://doi.org/10.1175/BAMS-85-3-381, 2004.

Rodell, M., Chen, J., Kato, H., Famiglietti, J. S., Nigro, J., and Wilson, C. R.: Estimating groundwater storage changes in the mississippi river basin (USA) using GRACE, Hydrogeol. J., 15, 159–166, https://doi.org/10.1007/s10040-006-0103-7, 2007.

Rodell, M., Velicogna, I., and Famiglietti, J. S.: Satellite-based estimates of groundwater depletion in India, Nature, 460, 999–1002, https://doi.org/10.1038/nature08238, 2009.

Rodell, M., Famiglietti, J. S., Wiese, D. N., Reager, J. T., Beaudoing, H. K., Landerer, F. W., and Lo, M.-H.: Emerging trends in global freshwater availability, Nature, 557, 651–659, https://doi.org/10.1038/s41586-018-0123-1, 2018.

Rohde, M. M., Albano, C. M., Huggins, X., Klausmeyer, K. R., Morton, C., Sharman, A., Zaveri, E., Saito, L., Freed, Z., Howard, J. K., Job, N., Richter, H., Toderich, K., Rodella, A.-S., Gleeson, T., Huntington, J., Chandanpurkar, H. A., Purdy, A. J., Famiglietti, J. S., Singer, M. B., Roberts, D. A., Caylor, K., and Stella, J. C.: Groundwater-dependent ecosystem map exposes global dryland protection needs, Nature, 632, 101–107, https://doi.org/10.1038/s41586-024-07702-8, 2024.

Rosseel, Y.: lavaan: An R package for structural equation modeling, Journal of Statistical Software, 48, 1–36, https://doi.org/10.18637/jss.v048.i02, 2012.

Save, H., Bettadpur, S., and Tapley, B. D.: High-resolution CSR GRACE RL05 mascons, J. Geophys. Res.: Solid Earth, 121, 7547–7569, https://doi.org/10.1002/2016JB013007, 2016.

https://doi.org/10.5194/egusphere-2026-2596
Preprint. Discussion started: 17 June 2026

Scanlon, B. R., Zhang, Z., Save, H., Wiese, D. N., Landerer, F. W., Long, D., Longuevergne, L., and Chen, J.: Global evaluation of new GRACE mascon products for hydrologic applications, Water Resources Research, 52, 9412–9429, https://doi.org/10.1002/2016WR019494, 2016.

Sen, P. K.: Estimates of the regression coefficient based on kendall's tau, J. Am. Stat. Assoc., 63, 1379–1389, https://doi.org/10.1080/01621459.1968.10480934, 1968.

Shamsudduha, M. and Taylor, R. G.: Groundwater storage dynamics in the world's large aquifer systems from GRACE: Uncertainty and role of extreme precipitation, Earth System Dynamics, 11, 755–774, https://doi.org/10.5194/esd-11-755-2020, 2020.

Shao, X., Gao, X., Cai, Y., Zhang, Z., Zhou, S., Tian, L., and Zhao, X.: Past precipitation stored in deep soils sustains greening of dryland tree plantations in northern China, Earth's Future, 13, e2025EF006181, https://doi.org/10.1029/2025EF006181, 2025.

Stelling, J. M., Slesak, R. A., Windmuller-Campione, M. A., and Grinde, A.: Effects of stand age, tree species, and climate on water table fluctuations and estimated evapotranspiration in managed peatland forests, J. Environ. Manage., 339, 117783, https://doi.org/10.1016/j.jenvman.2023.117783, 2023.

Sutanudjaja, E. H., van Beek, R., Wanders, N., Wada, Y., Bosmans, J. H. C., Drost, N., van der Ent, R. J., de Graaf, I. E. M., Hoch, J. M., de Jong, K., Karssenberg, D., López López, P., Peßenteiner, S., Schmitz, O., Straatsma, M. W., Vannametee, E., Wisser, D., and Bierkens, M. F. P.: PCR-GLOBWB 2: A 5 arcmin global hydrological and water resources model, Geosci. Model Dev., 11, 2429–2453, https://doi.org/10.5194/gmd-11-2429-2018, 2018.

Syed, T. H., Famiglietti, J. S., Rodell, M., Chen, J., and Wilson, C. R.: Analysis of terrestrial water storage changes from GRACE and GLDAS, Water Resour. Res., 44, 2006WR005779, https://doi.org/10.1029/2006WR005779, 2008.

Taylor, R. G., Scanlon, B., Döll, P., Rodell, M., Van Beek, R., Wada, Y., Longuevergne, L., Leblanc, M., Famiglietti, J. S., Edmunds, M., Konikow, L., Green, T. R., Chen, J., Taniguchi, M., Bierkens, M. F. P., MacDonald, A., Fan, Y., Maxwell, R. M., Yechieli, Y., Gurdak, J. J., Allen, D. M., Shamsudduha, M., Hiscock, K., Yeh, P. J.-F., Holman, I., and Treidel, H.: Ground water and climate change, Nat. Clim. Change, 3, 322–329, https://doi.org/10.1038/nclimate1744, 2013.

Ukasha, M., Ramirez, J. A., and Niemann, J. D.: Temporal Variations of NDVI and LAI and Interactions With Hydroclimatic Variables in a Large and Agro-Ecologically Diverse Region, JGR Biogeosciences, 127, e2021JG006395, https://doi.org/10.1029/2021JG006395, 2022.

Voss, K. A., Famiglietti, J. S., Lo, M., De Linage, C., Rodell, M., and Swenson, S. C.: Groundwater depletion in the middle east from GRACE with implications for transboundary water management in the tigris-euphrates-western iran region, Water Resour. Res., 49, 904–914, https://doi.org/10.1002/wrcr.20078, 2013.

Wang, J., Fu, B., Wang, L., Lu, N., and Li, J.: Water use characteristics of the common tree species in different plantation types in the loess plateau of China, Agric. For. Meteorol., 288–289, 108020, https://doi.org/10.1016/j.agrformet.2020.108020, 2020.

Wang, L., Jia, B., Yuan, X., Xie, Z., Yang, K., and Shi, J.: The slowdown of increasing groundwater storage in response to climate warming in the Tibetan Plateau, npj Clim Atmos Sci, 7, 286, https://doi.org/10.1038/s41612-024-00840-w, 2024.

Watkins, M. M., Wiese, D. N., Yuan, D., Boening, C., and Landerer, F. W.: Improved methods for observing Earth's time variable mass distribution with GRACE using spherical cap mascons, JGR Solid Earth, 120, 2648–2671, https://doi.org/10.1002/2014JB011547, 2015.

https://doi.org/10.5194/egusphere-2026-2596
Preprint. Discussion started: 17 June 2026

Wu, W.-Y., Lo, M.-H., Wada, Y., Famiglietti, J. S., Reager, J. T., Yeh, P. J.-F., Ducharne, A., and Yang, Z.-L.: Divergent effects of climate change on future groundwater availability in key mid-latitude aquifers, Nat Commun, 11, 3710, https://doi.org/10.1038/s41467-020-17581-y, 2020.

Xie, X., Liang, S., Yao, Y., Jia, K., Meng, S., and Li, J.: Detection and attribution of changes in hydrological cycle over the three-north region of China: Climate change versus afforestation effect, Agric. For. Meteorol., 203, 74–87, https://doi.org/10.1016/j.agrformet.2015.01.003, 2015.

Xie, X., Xu, C., Wen, Y., and Li, W.: Monitoring groundwater storage changes in the loess plateau using GRACE satellite gravity data, hydrological models and coal mining data, Remote Sens., 10, 605, https://doi.org/10.3390/rs10040605, 2018.

Xue, Z. and Ullrich, P. A.: Changing trends in drought patterns over the northeastern united states using multiple large ensemble datasets, J. Clim., 35, 7413–7433, https://doi.org/10.1175/JCLI-D-21-0810.1, 2022.

Yang, J. and Huang, X.: The 30 m annual land cover dataset and its dynamics in China from 1990 to 2019, Earth Syst. Sci. Data, 13, 3907–3925, https://doi.org/10.5194/essd-13-3907-2021, 2021.

Yang, W., Long, D., Scanlon, B. R., Burek, P., Zhang, C., Han, Z., Butler, J. J., Pan, Y., Lei, X., and Wada, Y.: Human intervention will stabilize groundwater storage across the north China plain, Water Resour. Res., 58, e2021WR030884, https://doi.org/10.1029/2021WR030884, 2022.

Yao, Y., Thiery, W., Ducharne, A., Cook, B. I., Ding, A., De Hertog, S. J., Sieber, P., Aas, K. S., Arboleda-Obando, P. F., Colin, J., Costantini, M., Decharme, B., Lawrence, D. M., Lawrence, P., Leung, L. R., Lo, M.-H., Devaraju, N., Wu, R.-J., Zhou, T., Jägermeyr, J., McDermid, S. S., Pokhrel, Y., Satoh, Y., Yokohata, T., Gudmundsson, L., and Seneviratne, S. I.: Irrigation-induced land water depletion aggravated by climate change, Nat. Water, 3, 1424–1435, https://doi.org/10.1038/s44221-025-00529-1, 2025.

Yin, X., Jiang, B., Chen, Y., Zhao, Y., and Tan, X.: Observational evidence highlights the spatial divergence of vegetation changes in altering land surface energy balance over the three-north region in China in summer, Ecol. Indic., 179, 114152, https://doi.org/10.1016/j.ecolind.2025.114152, 2025.

Zan, B., Ge, J., Mu, M., Sun, Q., Luo, X., and Wei, J.: Spatiotemporal inequality in land water availability amplified by global tree restoration, Nat Water, 2, 863–874, https://doi.org/10.1038/s44221-024-00296-5, 2024.

Zemp, D. C., Schleussner, C.-F., Barbosa, H. M. J., Hirota, M., Montade, V., Sampaio, G., Staal, A., Wang-Erlandsson, L., and Rammig, A.: Self-amplified amazon forest loss due to vegetation-atmosphere feedbacks, Nat Commun, 8, 14681, https://doi.org/10.1038/ncomms14681, 2017.

Zeng, J., Yuan, X., Yang, H., Ji, P., and Xu, X.: Characterizing flash drought patterns in eastern China based on high-resolution and long-term soil moisture fusion data, J. Hydrol., 661, 133680, https://doi.org/10.1016/j.jhydrol.2025.133680, 2025.

Zhang, J., Liesch, T., and Goldscheider, N.: Impacts of climate change and human activities on global groundwater storage from 2003 to 2022, J. Hydrol., 664, 134298, https://doi.org/10.1016/j.jhydrol.2025.134298, 2026.

Zhang, L., Li, X., Liu, X., Lian, Z., Zhang, G., Liu, Z., An, S., Ren, Y., Li, Y., and Liu, S.: Dynamic monitoring and drivers of ecological environmental quality in the three-north region, China: Insights based on remote sensing ecological index, Ecol. Inf., 85, 102936, https://doi.org/10.1016/j.ecoinf.2024.102936, 2025.

https://doi.org/10.5194/egusphere-2026-2596
Preprint. Discussion started: 17 June 2026

Zhang, Y., Peng, C., Li, W., Tian, L., Zhu, Q., Chen, H., Fang, X., Zhang, G., Liu, G., Mu, X., Li, Z., Li, S., Yang, Y., Wang, J., and Xiao, X.: Multiple afforestation programs accelerate the greenness in the 'three north' region of China from 1982 to 2013, Ecol. Indic., 61, 404–412, https://doi.org/10.1016/j.ecolind.2015.09.041, 2016.

Zhao, M., A, G., Zhang, J., Velicogna, I., Liang, C., and Li, Z.: Ecological restoration impact on total terrestrial water storage, Nat. Sustainability, 4, 56–62, https://doi.org/10.1038/s41893-020-00600-7, 2020.

Zheng, X., Zhu, J., Wang, G. G., Yan, Q., Sun, T., Song, L., Gao, T., Sun, Y., Li, X., Yang, K., Zhang, J., Yu, L., Qi, K., Zhao, L., Lu, D., and Lu, Z.: Assessing the ecological effects of the world's largest forestry eco-engineering: Three-north protective forest program within the initially scheduled range from 1978 to 2022, Sci. China Life Sci., 68, 314–327, https://doi.org/10.1007/s11427-024-2705-4, 2025.

Zhu, E., Wang, Y., and Yuan, X.: Changes of terrestrial water storage during 1981–2020 over China based on dynamic-machine learning model, J. Hydrol., 621, 129576, https://doi.org/10.1016/j.jhydrol.2023.129576, 2023.

Zomer, R. J., Xu, J., and Trabucco, A.: Version 3 of the global aridity index and potential evapotranspiration database, Sci. Data, 9, 409, https://doi.org/10.1038/s41597-022-01493-1, 2022.

Zou, Y., Kuang, X., Feng, Y., Jiao, J. J., Liu, J., Wang, C., Fan, L., Wang, Q., Chen, J., Ji, F., Yao, Y., and Zheng, C.: Solid Water Melt Dominates the Increase of Total Groundwater Storage in the Tibetan Plateau, Geophysical Research Letters, 49, e2022GL100092, https://doi.org/10.1029/2022GL100092, 2022.

https://doi.org/10.5194/egusphere-2026-2596
Preprint. Discussion started: 17 June 2026

Figures

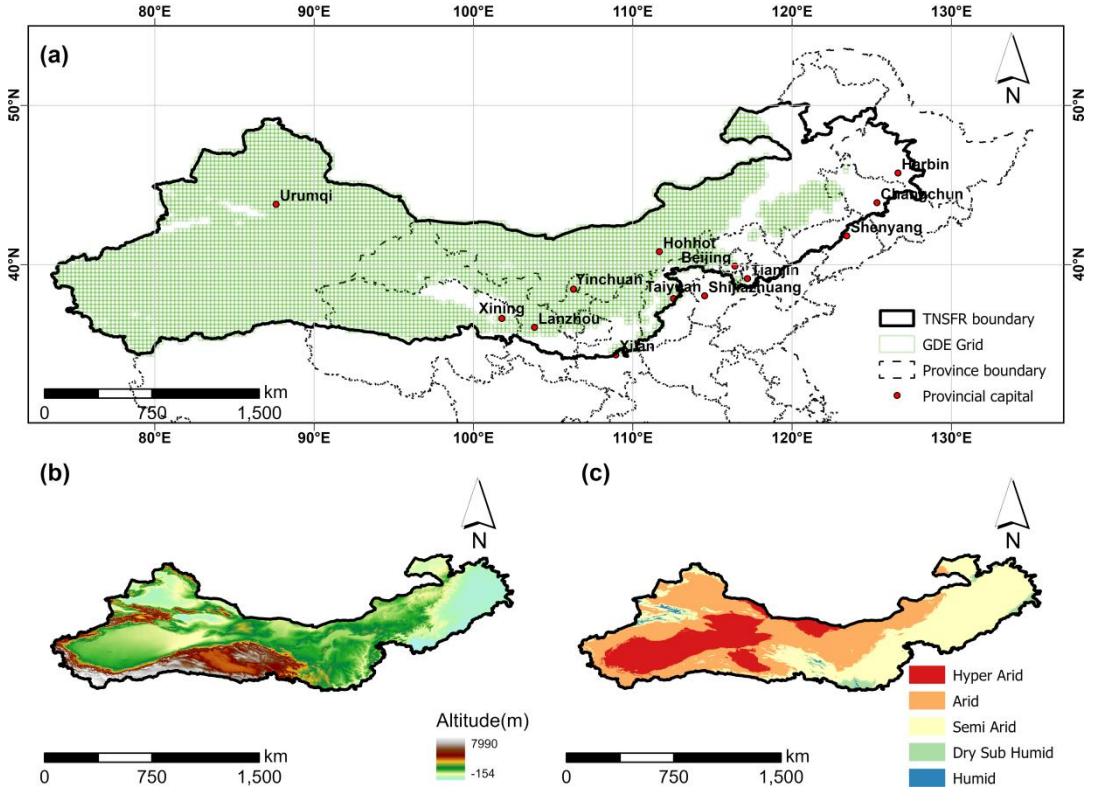

665 **Figure 1** Overview of the Three-North Shelter Forest Region (TNSFR). (a) Geographical location of TNSFR. (b) Elevation map. (c) Climate zone map.

https://doi.org/10.5194/egusphere-2026-2596
Preprint. Discussion started: 17 June 2026

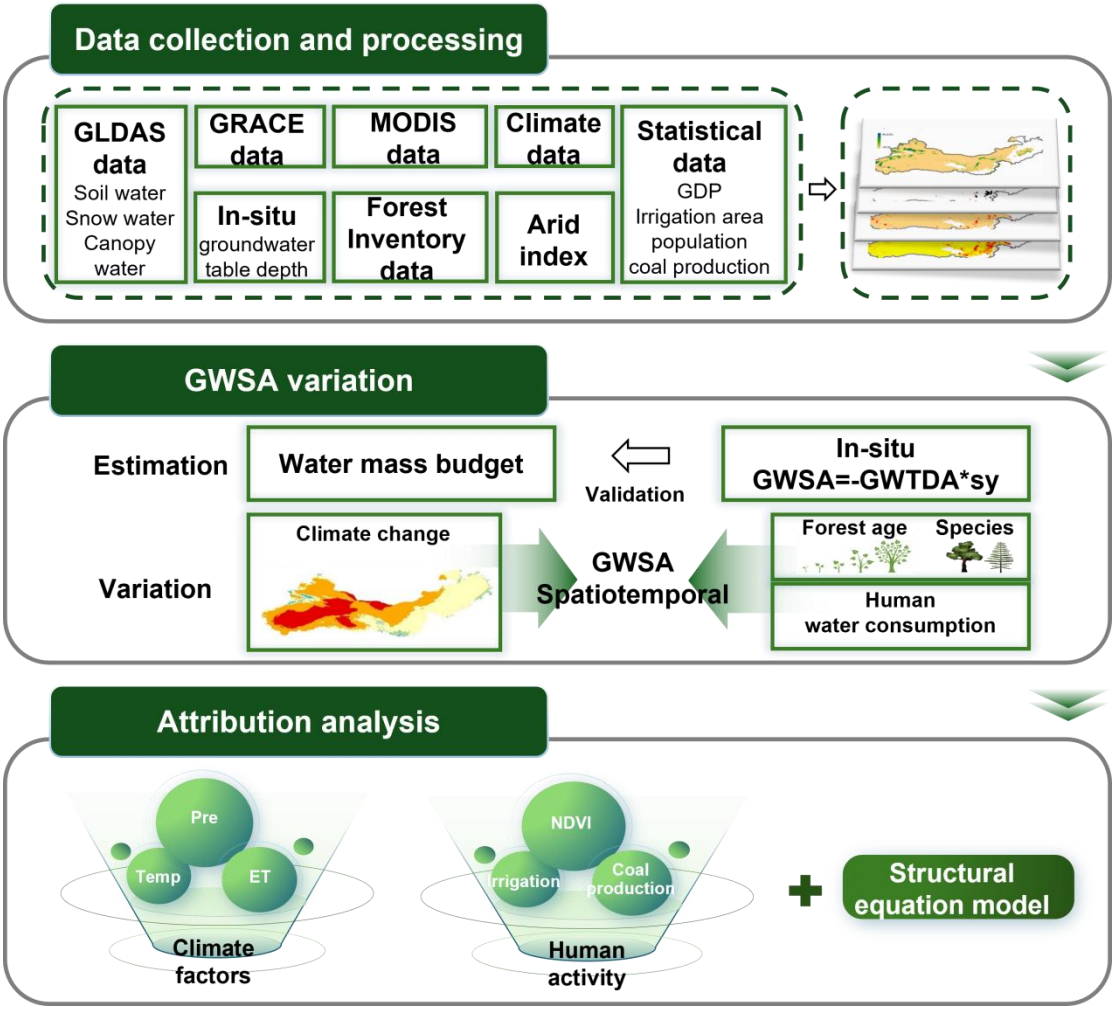

Figure 2 Flowchart illustrating the analytical procedures carried out in this study.

670

https://doi.org/10.5194/egusphere-2026-2596
Preprint. Discussion started: 17 June 2026

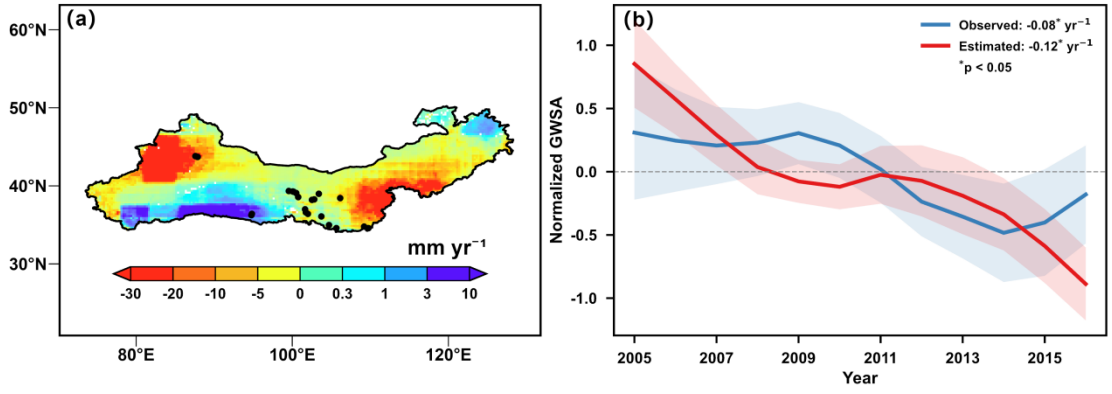

Figure 3 Groundwater storage anomaly (GWSA) trends in the TNSFR. (a) Spatial distribution of GWSA trends during 2003–2023. Black dots represent locations of groundwater monitoring wells used for validation. (b) Time series of normalized GWSA averaged across monitoring wells, comparing observations (blue) and estimated values (red), with the significance of these rates listed at the 0.05 level

https://doi.org/10.5194/egusphere-2026-2596
Preprint. Discussion started: 17 June 2026

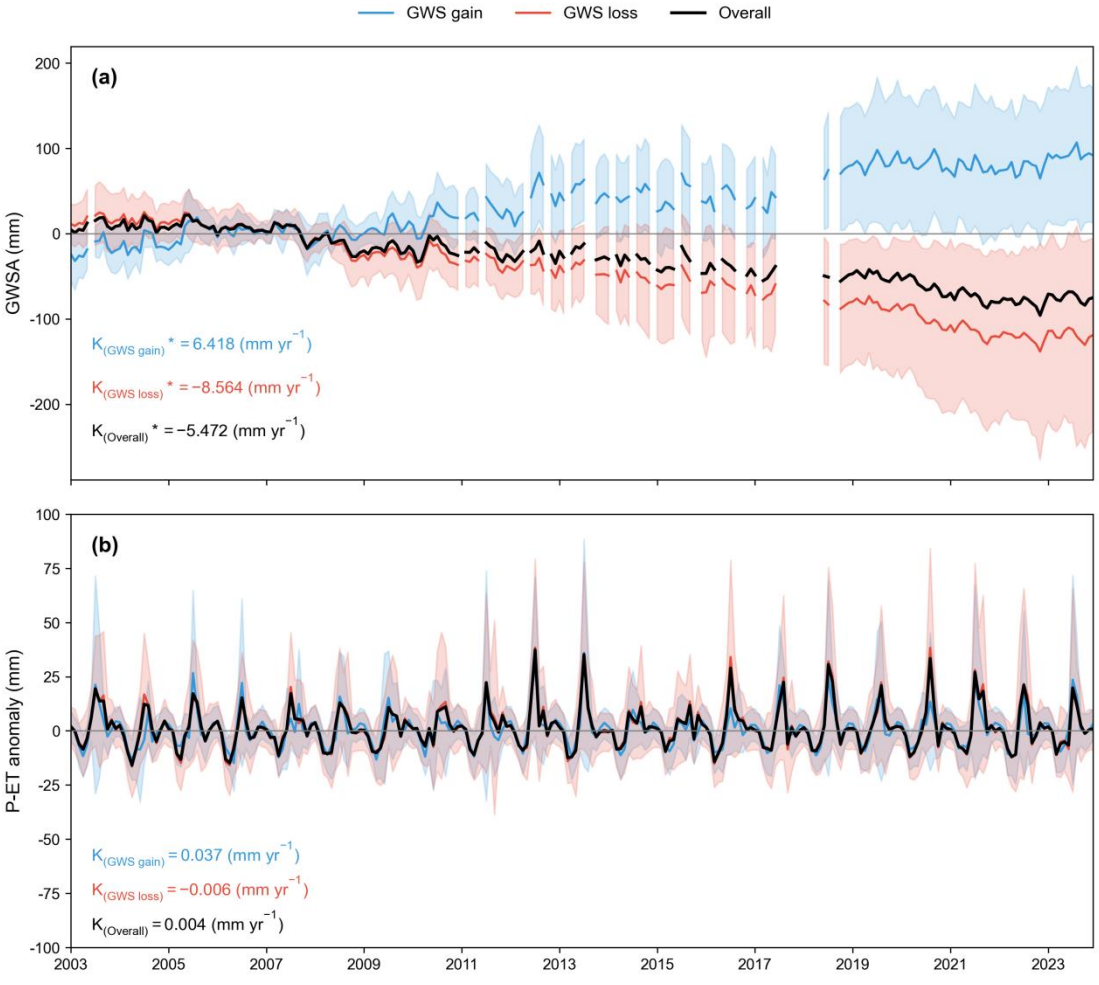

Figure 4 (a) Monthly time series of GWSA from 2003 to 2023; (b) Monthly time series of P-ET anomaly over the same period. The red line shows the average GWS loss trend, the blue line shows the average GWS gain trend, and the black line represents the overall TNSFR average. (* denotes $p < 0.05$).

https://doi.org/10.5194/egusphere-2026-2596
Preprint. Discussion started: 17 June 2026

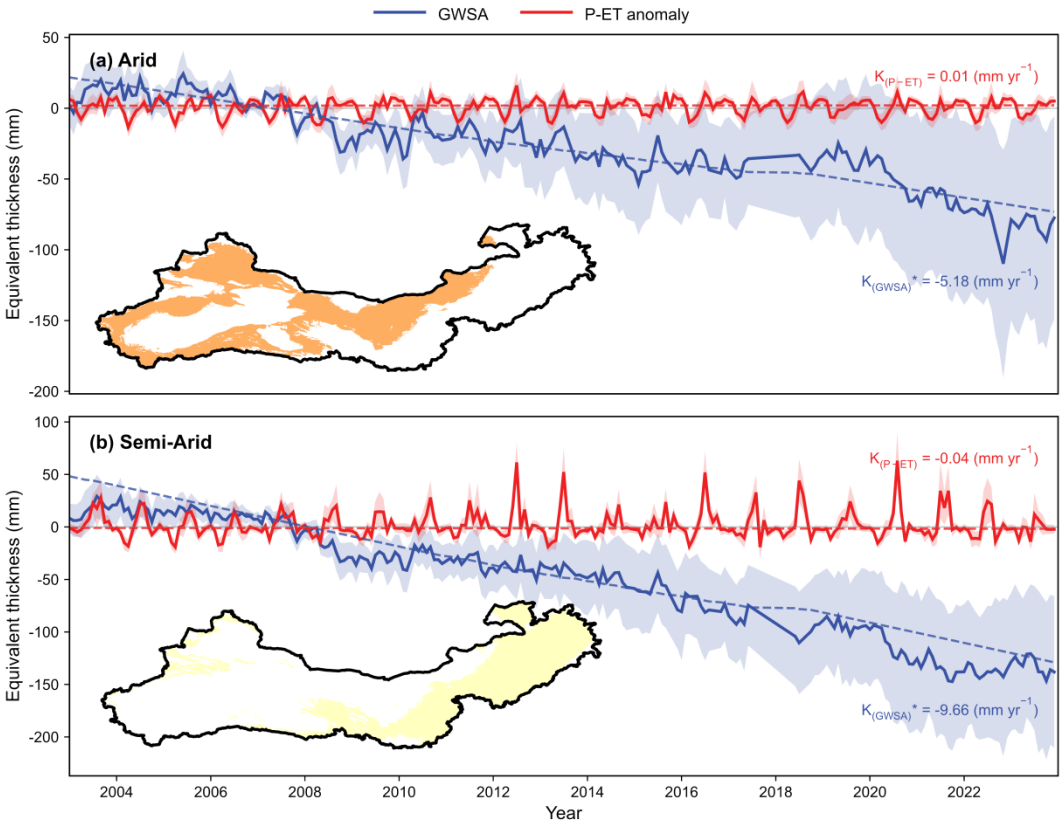

Figure 5 Monthly time series of GWSA and P-ET anomaly in the arid (a) and semi-arid (b) zones of the TNSFR during 2003-2023. Dashed lines indicate linear trends.

https://doi.org/10.5194/egusphere-2026-2596
Preprint. Discussion started: 17 June 2026

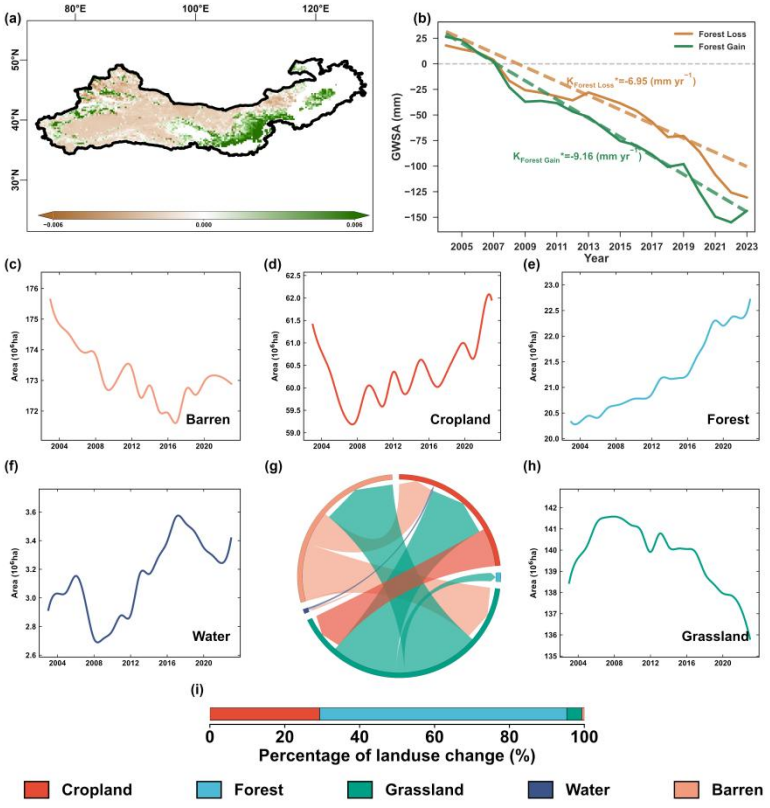

Figure 6 Impact of vegetation change on GWSA in the TNSFR during 2003–2023 (a) NDVI trends. (b) GWSA time series in forest gain and loss areas. Dashed lines indicate linear trends. (c-f, h) Area changes in cropland, forest, grassland, water, barren land. (g) Transition dynamics of land. (i) Percentage of land use change.

https://doi.org/10.5194/egusphere-2026-2596
Preprint. Discussion started: 17 June 2026

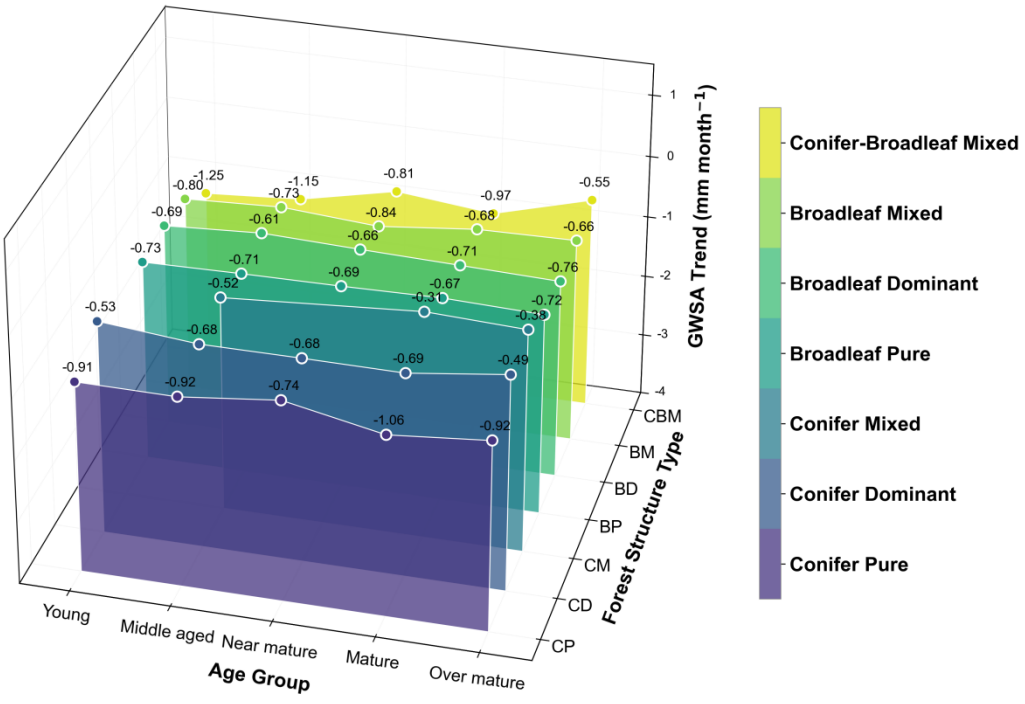

Figure 7 GWSA trends across different forest structure types and age groups in the TNSFR. Forest structure types include conifer pure (CP), conifer dominant (CD), conifer mixed (CM), broadleaf pure (BP), broadleaf dominant (BD), broadleaf mixed (BM), and conifer-broadleaf mixed (CBM). Age groups are classified as young, middle aged, near mature, mature, and over mature.

https://doi.org/10.5194/egusphere-2026-2596
Preprint. Discussion started: 17 June 2026

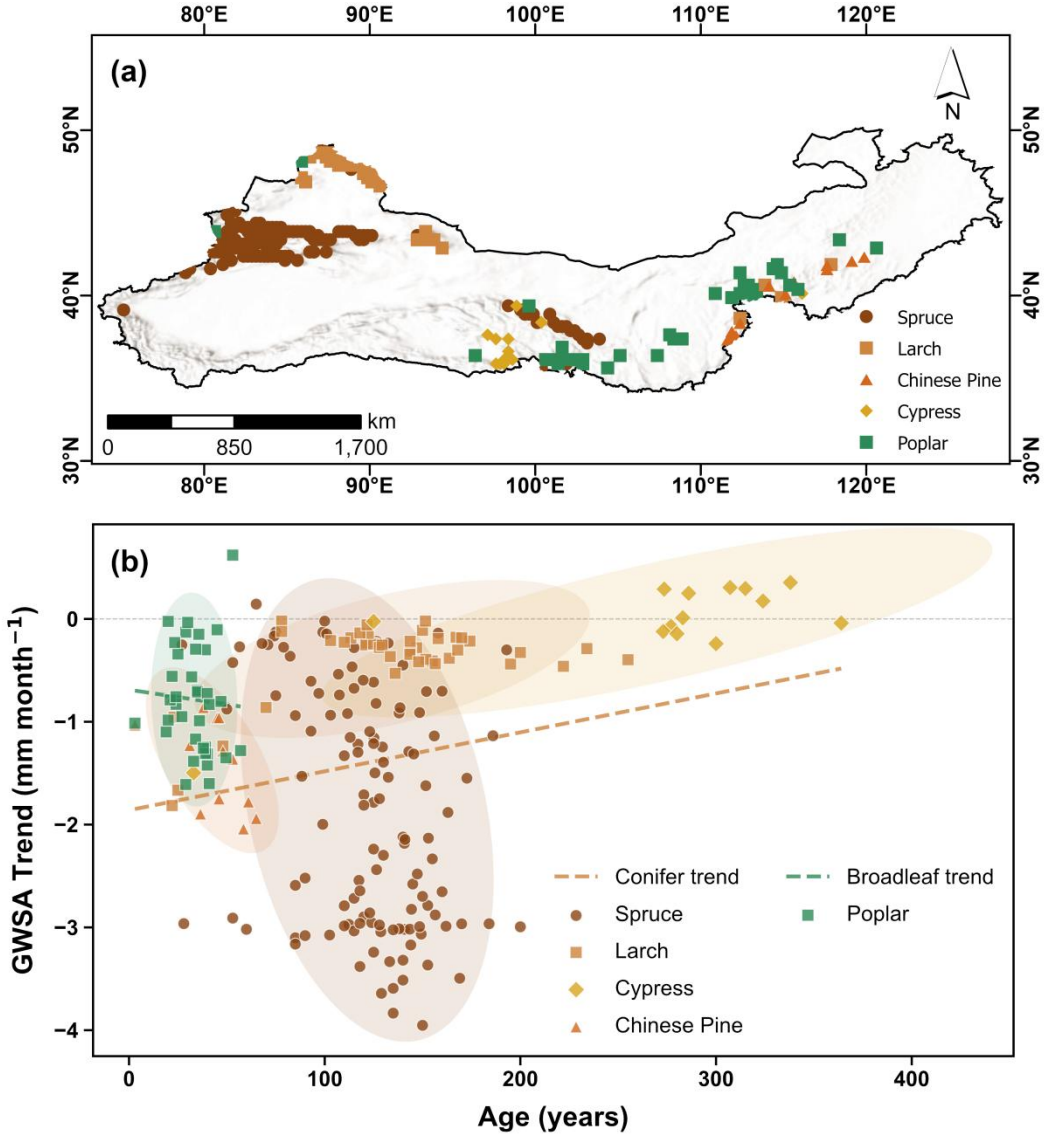

Figure 8 Dominant tree species distribution and their relationship with GWSA trends in the TNSFR. (a) Spatial distribution of dominant species in monospecific plots. (b) Relationship between stand age and GWSA trends. Ellipses indicate species distribution ranges; dashed lines show overall trends for coniferous (orange) and broadleaf (green) forests.

https://doi.org/10.5194/egusphere-2026-2596
Preprint. Discussion started: 17 June 2026

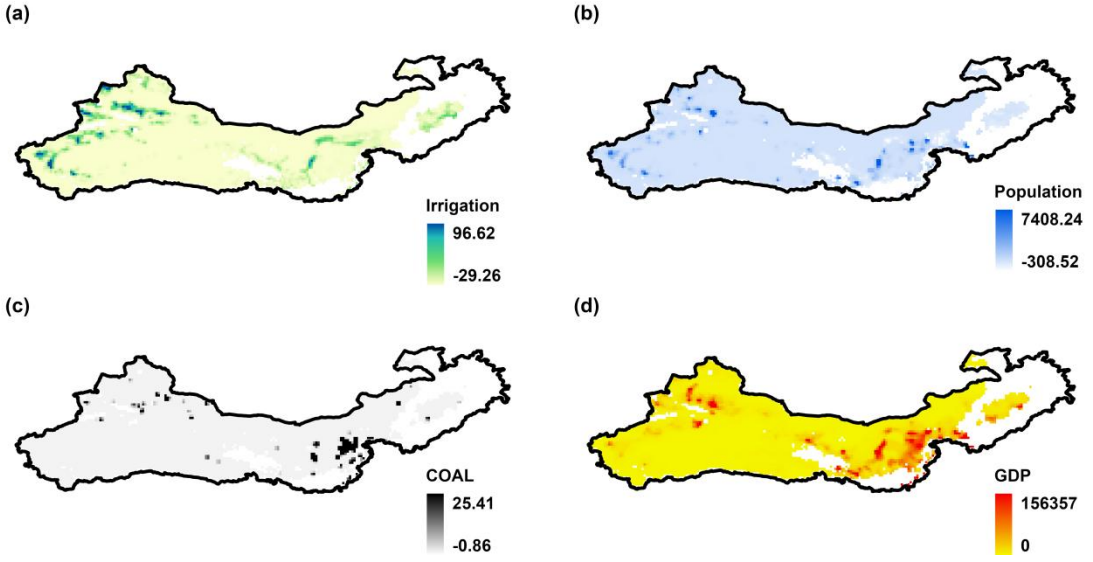

Figure 9 Map of anthropogenic activity trends in the TNSFR from 2003 to 2023. (a) Trends in irrigated area (103 ha yr^{-1}). (b) Trends in population (persons yr^{-1}). (c) Trends in coal production (10^4 tons yr^{-1}). (d) Trends in gross domestic product (10^4 yuan yr^{-1}).

https://doi.org/10.5194/egusphere-2026-2596
Preprint. Discussion started: 17 June 2026

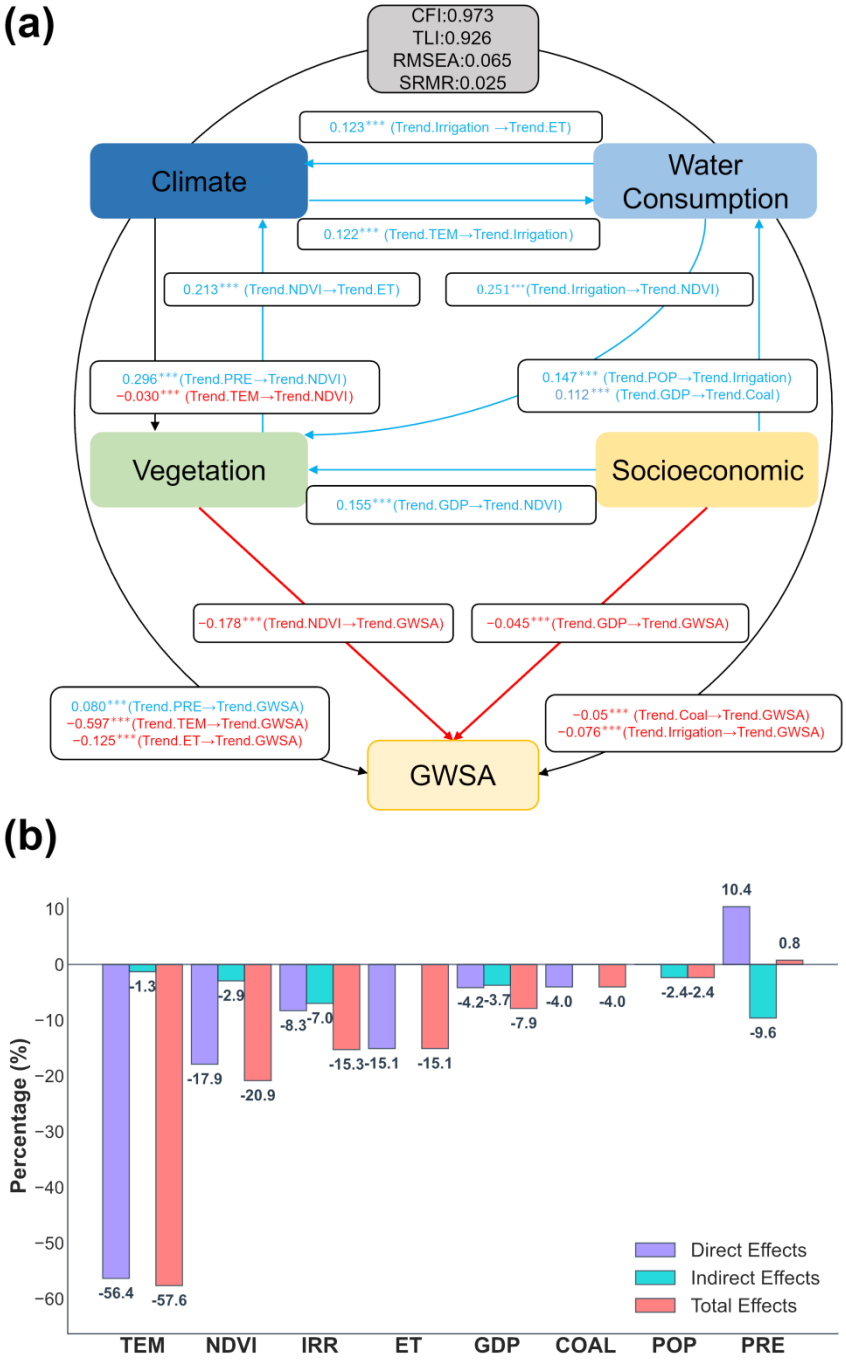

Figure 10 SEM analysis of driving factors affecting GWSA. (a) Path diagram showing relationships among climate, water consumption, vegetation, socioeconomic factors, and GWSA. Model fit: CFI = 0.973, TLI = 0.926, RMSEA = 0.065, SRMR = 0.025. (b) Contributions of driving factors to GWSA: direct, indirect, and total effects.